

© SHUTTERSTOCK/TITIMA ONGKANTONG

Rearrange Anatomy Inputs Like LEGO Bricks: Applying InSSS-P and a Mobile-Dense Hybrid Network to Distill Vascular Significance From Retina OCT-Angiography

Kao-Jung Chang ^{ID}, **Tai-Chi Lin** ^{ID},
Chih-Chien Hsu ^{ID}, **De-Kuang Hwang** ^{ID},
Shih-Jen Chen ^{ID}, and **Shih-Hwa Chiou** ^{ID}
National Yang Ming Chiao Tung University, TAIWAN and
also Taipei Veteran General Hospital, TAIWAN

Cheng-Yi Li and Ling Chen ^{ID}
National Yang Ming Chiao Tung University, TAIWAN

Cherng-Ru Hsu ^{ID}
Show Chwan Memorial Hospital, TAIWAN

Wei-Hao Chang
Acer Medical Inc., TAIWAN

Digital Object Identifier 10.1109/MCI.2024.3401348
Date of current version: 12 July 2024

This article was recommended for publication by Associate Editor Min Jiang.
Corresponding author: Shih-Hwa Chiou (e-mail: shchiou@vghtpe.gov.tw).

Abstract—Medical deep neural networks (DNNs) trained upon coarse image inputs are inherently insensible to fine-grained anatomic features. To enhance DNN perception on delicate microvascular structures, we proposed using a straightforward angiographic mobile-dense hybrid network (AMDenseNet) in tandem with a flexible input split, suppression, and swap perturbation (InSSS-P) framework to perform explainable diagnostics for microvascular diseases. Mechanistically, InSSS-P and AMDenseNet conjointly (1) decompose complex anatomy inputs into LEGO-like blocks, then (2) distill plexus-wise vascular block significance from the rearranged anatomy input-output samplings. To validate the robustness of the proposed model, we trained AMDenseNet to detect blind-threatening retina exudative age-related macular degeneration (exAMD) from the micrometer-scaled optic coherence tomographic angiography (OCTA), wherein our AMDenseNet annotated triple-specific (plexus, branch, and exudate activity) neovascular (NV) features at a diagnostic precision that is comparable to the gold standard dye-based angiography. Interestingly, when we applied plexus-wise InSSS-P to the AMDenseNet predictions, the permuted results demonstrated that input perturbation at deep capillary plexus (DCP) layer abrogated model-aware exAMD features and resulted in false-negative exAMD impressions. On the contrary, choroid capillary (CC) input perturbations contributed to false-positive exAMD characterization. Notably, the AMDenseNet triple-specific NV annotation functionality was disrupted by either DCP or CC input perturbations, indicating the significance of DCP and CC in the task of exAMD characterization. In sum, this study employed anatomy decomposition approaches to distill plexus-wise microvascular significance and highlighted the analytic potential of leveraging an anatomy-sensible model to discover novel disease biomarkers.

I. Introduction

Medical deep neural networks (DNNs) have renovated healthcare industry through advancing frontiers in image diagnostics [1], [2], drug development [3], [4], and digital pathology [5], [6]. However, the clinical implementation of medical DNN was hindered by the European Union (EU) General Data Protection Regulation (GDPR, Article No. 13-15; 21-22), which the article stated that all automated products were responsible for providing clear explanation on how the decision process was formed, namely, the clinical relevance in regard to the medical realm [7], [8], [9]. Henceforth, creating an explainable artificial intelligence (xAI) with clinical sense has become a high priority for medical DNN developers.

A. The Perturbation-Based Explainability of DNNs

The essential task of developing medical xAI was to link input image features to output model decisions [10], [11], by which the mainstream techniques include perturbation-based methods (PBMs) and the gradient-based methods. While the gradient-based methods deduct model explainability from the gradient loss within

the DNN black box, PBMs attribute feature importance through input-output sampling that works independently from the black box interior [12], [13]. Under a fixed convolution model, PBMs monitor the interlocked changes between the input perturbations and the output decays. Therefore, the significance of a target input can be inferred by the degree of model performance loss.

Some representative PBM-xAI techniques include occlusion [14], RISE [15], LIME [16], kernel SHAP [17], and ROAR [18], all of which assess feature significance by measuring the marginal contribution of piecemeal input information. Although input targeting PBMs have been broadly applied to various research trajectories, in this study, we focused on whether the input targeting PBMs could distill clinically-significant features from medical DNNs working in a complex anatomical context.

B. Input Perturbation (InP) in Medical Images

General input perturbation (InP) experiments are often blocking pixels of an image, changing a phrase in a sentence or removing a fragment of a video clip, whereas the perturbation designs in the medical domain are primarily disrupting the anatomical location, lesion texture details, organ edges, vascular signals and other miscellaneous recessive features [19].

Vascular pixel erasure was a particular perturbation strategy that has been leveraged to study model decisions in vascular diseases such as age-related macular degeneration (AMD) [20] and Alzheimer's disease [21]. In these two cases, perturbation of the retinal choroid vascular bed and the amyloid-beta loaded brain vessels resulted in reduced model prediction accuracy. This indicated that different diagnostic tasks rely context-dependent vascular features to make optimal characterizations. Therefore, vascular targeting InPs beheld the key to the clinical explainability of model decision.

Occlusion-based InPs embodies the backbone of various medical xAI strategies [22]; however, occlusion masks are often rigid in shape, lack of design flexibility, and are unaware of long-range features. Therefore, occlusion-based InPs often fall short to address local curvilinear anatomy features [23]. In this regard, it is hard to adapt general grid-based InPs to the non-homogenous sterical-expressive microvascular images [24]. Moreover, recent studies [25], [26], [27], [28] reported that PBM-derived xAI was not robust enough to withstand small variations in the perturbation process. In the study context of retinal microvasculature, the objective limits of PBM-xAIs introduce analytic uncertainty to the profiling of the spatiotemporal (different retina layers and disease stages) retina conditions. Therefore, it was imperative to invent a robust InP strategy to harness the microscopic features of the retina microvasculature.

C. The Potential and Challenges of OCTA Clinical Use

Microvascular degeneration is the hallmark feature of many blindness diseases including age-related macular degeneration (AMD) [29] [30]. The implementation of optical coherence tomography angiography (OCTA) provides exact visualization on the depth-resolved microvasculature structures, which the non-invasive OCTA protocol circumvents the dye injection side effects in the traditional fluorescein and indocyanine angiography [31].

Canonically, retina vasculatures are presented into four physiological plexuses (from vitreous to sclera: superficial capillary plexus; SCP, deep capillary plexus; DCP, outer retina; OR and choroid capillary; CC) on OCTA reports. Spatially, the SCP and DCP run within the retina, whereas the CC runs beneath the retina, and OR represents the avascular segment at the photoreceptor layer. Each vascular plexus presents unique angiomorphic features under physiological and pathological conditions; therefore, investigating microvascular morphology can facilitate disease pattern recognition [29], [32].

Quantitative OCTA markers (vascular density, perfusion density, vascular caliber, foveal avascular zone, branching index, fractal dimension, and entropy) [33], [34] and qualitative descriptions (vascular loops, peripheral anastomotic arcades, and choriocapillaris hypo-intense halo) [35], [36] have been utilized to diagnose AMD with a documented positive predictive value of 87.9% [37], [38], [39], [40]. However, biomarker processing in OCTA is low-throughput, labor intensive, and prone to interoperator bias; these technical barriers collectively reduce the diagnostic value of OCTA [41]. In this regard, DNNs can be implemented to propel end-to-end OCTA analysis in clinical care.

D. DNN Application in OCTA Images

Implementing DNNs in OCTA images has enhanced OCTA diagnostics in four directions: artifact improvement, interlayer plexus segmentation, artery-vein discrimination, and intra-layer lesion segmentation [42], [43], [44], [45], [46], [47], [48].

In the early years of OCTA application, micrometer-scaled angiographic pixels were vulnerable to eye motion artifacts; therefore, models such as disentangled representation learning (DRL) [49], [50] and RCV-Net [51] were applied to realign defective OCTA scans and restore fuzzy signals, respectively. Retinal fluid accumulation, on the other hand, also impairs image quality by disrupting natural plexus borders [52], upon which the boundary shape and distance aware joint learning framework (BSDA-Net) and other akin models were proposed to reconstruct indistinctive OCTA plexus borders [53], [54], [55]. With the advance of DNN models, variable quality control tools have been developed to perform OCTA image sanity checks [56], [57], [58], [59].

To extract vascular features from retinal OCTA images, feature annotation and lesion segmentation models were also developed in recent years. Currently, DNN-based models have been applied to segment retinal arteries, veins, avascular zones, and nonperfusion areas, and these OCTA biomarkers can be further utilized for retinopathy characterization. To be specific, AV-Net-based models [60], [61], [62] can differentiate arterioles from venules, and provides critical artery and vein annotation for retinal artery and retinal vein occlusions (RAO; RVO) diagnosis. Other U-Net [63], [64], multiscale encode-decoder (MED-Net) and voting-based adaptive feature fusion (VAFF-Net) [65] models were also developed to assess OCTA angiomorphic biomarkers (focal avascular zone; FAZ, nonperfusion area and vascular branching points). These

DNN-derived biomarker studies have promoted OCTA diagnostics in RVO [66], DR [67], and AMD [68].

E. Purpose and Contribution of This Study

While previous DNN studies have focused on segmenting intra-plexus crude features (FAZ at the SCP; NV at the OR plexus), this study aims to propose an anatomy-sensible model that possesses balanced attention across both the plexus-by-plexus retinal conditions (global) and the branch-specific vascular features (local).

To digest the local pixel details without sacrificing long range attention on the global anatomic patterns, we customized a straightforward angiographic mobile-dense hybrid neuron network (AMDenseNet) that functions sensibly to both the intra-plexus (NV branches) and the inter-plexus (four OCTA layers) vascular signatures (Figure 1(a)). Notably, we demonstrated that the xAI results of the AMDenseNet are clinically relevant and can discriminate three important NV features (plexus depth, vascular branches, and leakage activity) at a comparable quality of dye-based angiography gold standards.

Based on the mobile-dense hybrid network, we further proposed a pluggable input split, suppress, and swap perturbation (InSSS-P) framework that generates input-output sample pairs by rearranging anatomical inputs like LEGO blocks. By assessing the marginal gain and loss of the output performance, we may backward infer the selected anatomic significance through manipulating the presence and absence of particular vascular input (Figure 1(b)). Moreover, InSSS-P consists of three independent split, suppress, and swap actions which can be leveraged to study feature necessity, dependence and dominance.

Our primary findings addressed the pressing needs of employing anatomy-sensible models for medical diagnostics. To our knowledge, this is the first study that employs modified input perturbation alongside a hybrid DNN to distill plexus-specific vascular significance from retinal OCTA images.

II. Materials and Methods

A. Ethical and Information Use Approval

The metadata used in this study were collected and deidentified by the Big Data Center, Taipei Veterans General Hospital (BDC, TVGH). The process was approved and supervised by the Institutional Review Board of Taipei Veterans General Hospital in accordance with the Declaration of Helsinki.

B. Clinical Context and Model Applicability

This study employed a DNN and OCTA images to identify treatable AMD patients via a two-tier task (Figure 2(a)). The first task is to detect neovascular (NV) lesions, and the second task is to determine the exudative status of the NV lesions. Treatment may be indicated for patients with NV lesions with exudative activity (exAMD), whereas NV lesions with no exudation (qAMD) require close follow-up. Using a DNN and OCTA images, we aimed to provide a noninvasive diagnostic framework with angiomorphic insights for AMD assessment.

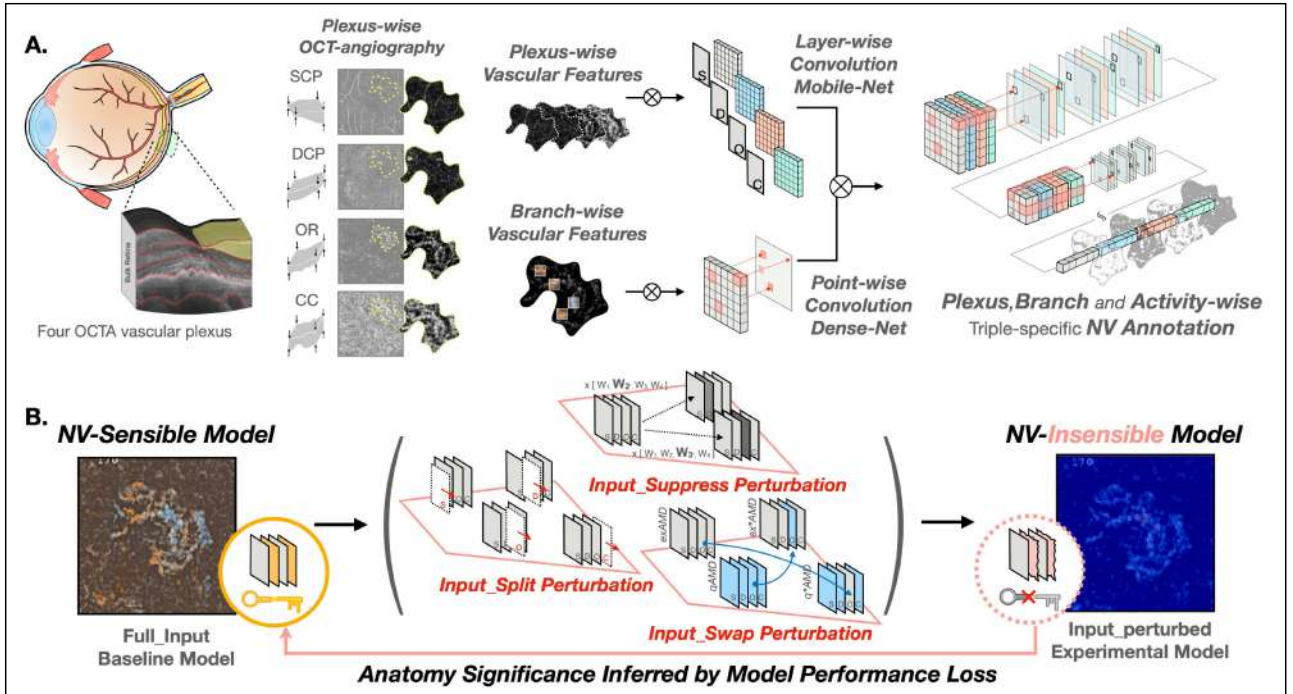


FIGURE 1 Schematic structure of the study design. (A) Depth-resolved vascular OCTA images were obtained to train the plexus-wise feature-sensible model for neovascular characterization. To fully explore the plexus-wise and branch-wise diagnostic value of the vascular features, we combined layer-wise MobileNet with point-wise DenseNet to foster a triple-specific (plexus, branch, and activity) NV-sensible model. (B) Based on the NV-sensible model, we further applied an ante-hoc input split, suppress, and swap perturbation (InSSS-P) module to assess the perturbation coupling model performance loss.

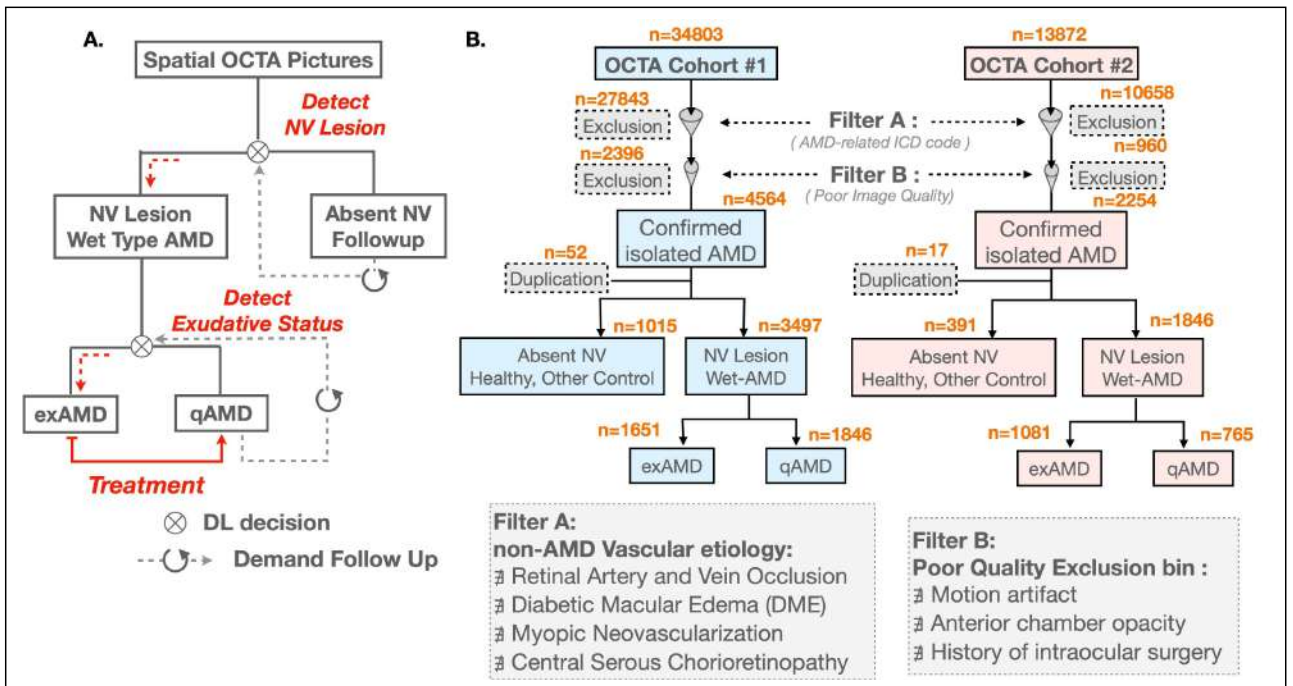


FIGURE 2 The DNN decision flowchart in AMD characterization and the clinical cohort collection for model training. (A) The model was trained to achieve two-stage AMD characterization including tasks of NV detection (AMD vs. non-AMD) and exudation detection (exAMD vs. qAMD). (B) The workflow of data collection, cleaning, and labeling in two independent OCTA cohorts. A total of 3497 and 1846 neovascular AMD OCTA pictures were collected in cohort #1 and cohort #2, respectively.

TABLE I The hybrid model structure of AMDenseNet.

LAYERS	OUTPUT SIZE	DENSENET-121	AMDNET
CONVOLUTION LAYER	112 × 112		7 × 7 conv, stride 2
POOLING LAYER	56 × 56	$\begin{bmatrix} 1 \times 1 \text{ conv} \\ 3 \times 3 \text{ conv} \end{bmatrix} \times 6$	3 × 3 max pool, stride 2
DENSE BLOCK(1)	56 × 56		$\begin{bmatrix} 1 \times 1 \text{ conv} \\ 3 \times 3 \text{ depthwise separable conv} \\ 1 \times 1 \text{ conv} \end{bmatrix} \times 3$
	56 × 56		2 × 2 average pool, stride 2
TRANSITION LAYER(1)	28 × 28	$\begin{bmatrix} 1 \times 1 \text{ conv} \\ 3 \times 3 \text{ conv} \end{bmatrix} \times 12$	$\begin{bmatrix} 1 \times 1 \text{ conv} \\ 3 \times 3 \text{ depthwise separable conv} \\ 1 \times 1 \text{ conv} \end{bmatrix} \times 6$
DENSE BLOCK(2)	28 × 28		
	28 × 28		2 × 2 average pool, stride 2
TRANSITION LAYER(2)	14 × 14	$\begin{bmatrix} 1 \times 1 \text{ conv} \\ 3 \times 3 \text{ conv} \end{bmatrix} \times 24$	$\begin{bmatrix} 1 \times 1 \text{ conv} \\ 3 \times 3 \text{ depthwise separable conv} \\ 1 \times 1 \text{ conv} \end{bmatrix} \times 12$
DENSE BLOCK(3)	14 × 14		
	14 × 14		2 × 2 average pool, stride 2
TRANSITION LAYER(3)	7 × 7	$\begin{bmatrix} 1 \times 1 \text{ conv} \\ 3 \times 3 \text{ conv} \end{bmatrix} \times 16$	$\begin{bmatrix} 1 \times 1 \text{ conv} \\ 3 \times 3 \text{ depthwise separable conv} \end{bmatrix} \times 8$
DENSE BLOCK(4)	7 × 7		7 × 7 global average pool
CLASSIFICATION LAYER	1 × 1		

C. Image Acquisition and Labeling

To establish model training materials, meta-data of two zero overlap AMD cohorts (International Classification of Diseases-9 codes H35.30, H35.31, and H35.32) were collected. OCTA and other associated retinal images were downloaded from the UniWeb server that was maintained by the Department of Ophthalmology, Taipei Veterans General Hospital.

OCTA images were obtained using the RTVue XR Avanti system (OptoVue). The regions of interest (ROIs) were fixed to the 3x3 mm window of the central retina. All four retina plexuses—the superficial capillary plexus (SCP), deep capillary plexus (DCP), outer retina (OR) and choroid capillaris (CC)—were segmented and visualized by model intrinsic split-spectrum amplitude decorrelation angiography (SSADA). By default, the OCTA report had an eight-figure layout with four retina plexuses depicted in vascular and structural mode. Only vascular module images were cropped and bilinearly downsampled to 304*304, and the image pixel range was reset from 0–255 to 0–1.

Patients with non-AMD etiology (Figure 2(b), filter A), duplication exams and patients with poor image quality (Figure 2(b), filter B) were excluded from this study. All OCTA images were reviewed and labeled by a retinal specialist committee, yielding 2732 exAMD patients (n = 1651 in cohort 1, n = 1081 in cohort 2), 2611 qAMD patients (n = 1846 in cohort 1, n = 765 in cohort 2), and 1406 control patients (n = 1015 in cohort 1, n = 391 in cohort 2).

D. Model Selection for Spatial Neovascular Anatomy

To fully exploit the 2.5-dimensional diagnostic value of the OCTA data, we constructed an angiographic mobile-dense hybrid neuron network (AMDenseNet) that combines depth-wise convolution from MobileNet [69] and point-wise convolution from DenseNet [70]. Functionally, the layer-wise convolution processes the plexus-wise global retinal structure, while the point-wise convolution addresses the branch-wise local vascular details.

The AMDenseNet was benchmarked against two standard models: EfficientNet [71] and ResNet [72]. Five-fold validation and data augmentation were used during training. Adaptive moment estimation (Adam) [73] and categorical cross-entropy were applied to optimize the loss function. The hybrid model structure is shown in Table I.

All the models were trained to perform two-tier tasks: first to detect the NV structure, followed by determining the NV exudation activity. The model performance was evaluated by a matrix consisting of the accuracy, sensitivity, specificity and F1-score. Model attention was visualized by axiom attribution [74] and then validated by multimodal retinal images, including the gold standard dye-based angiography.

E. Input Split, Suppression and Swap Perturbations

Input perturbation (InP) is a pre-convolution process that disrupts target-specific input information. In this study, we tested the applicability of different perturbation methods and maximized the InP operability by rearranging anatomical inputs into LEGO-like bricks.

To investigate the contribution of the asymmetric OCTA plexus to NV diagnosis, we applied split, suppress, and swap input perturbations to delineate the anatomical significance of these perturbations in model decisions.

1) *Input Split Perturbation*: Only three out of the complete four OCTA plexus images were channeled into layer-wise model convolutions.

$$\#(In_{SCP}, In_{DCP}, In_{OR}, In_{CC}) \rightarrow (\mathbf{x}, In_{DCP}, In_{OR}, In_{CC})$$

2) *Input Suppression Perturbation*: One of the four plexus images was subjugated to a grayscale weighted gradient ($\mathbf{w} = 0.8, 0.6, 0.4, 0.2, \text{ and } 0$)

$$\#(In_{SCP}, In_{DCP}, In_{OR}, In_{CC}) \rightarrow (In_{SCP} * \mathbf{w}, In_{DCP}, In_{OR}, In_{CC})$$

3) *Input Swap Perturbation*: For the same patient, two disease status (exAMD and qAMD) image pairs were collected, and

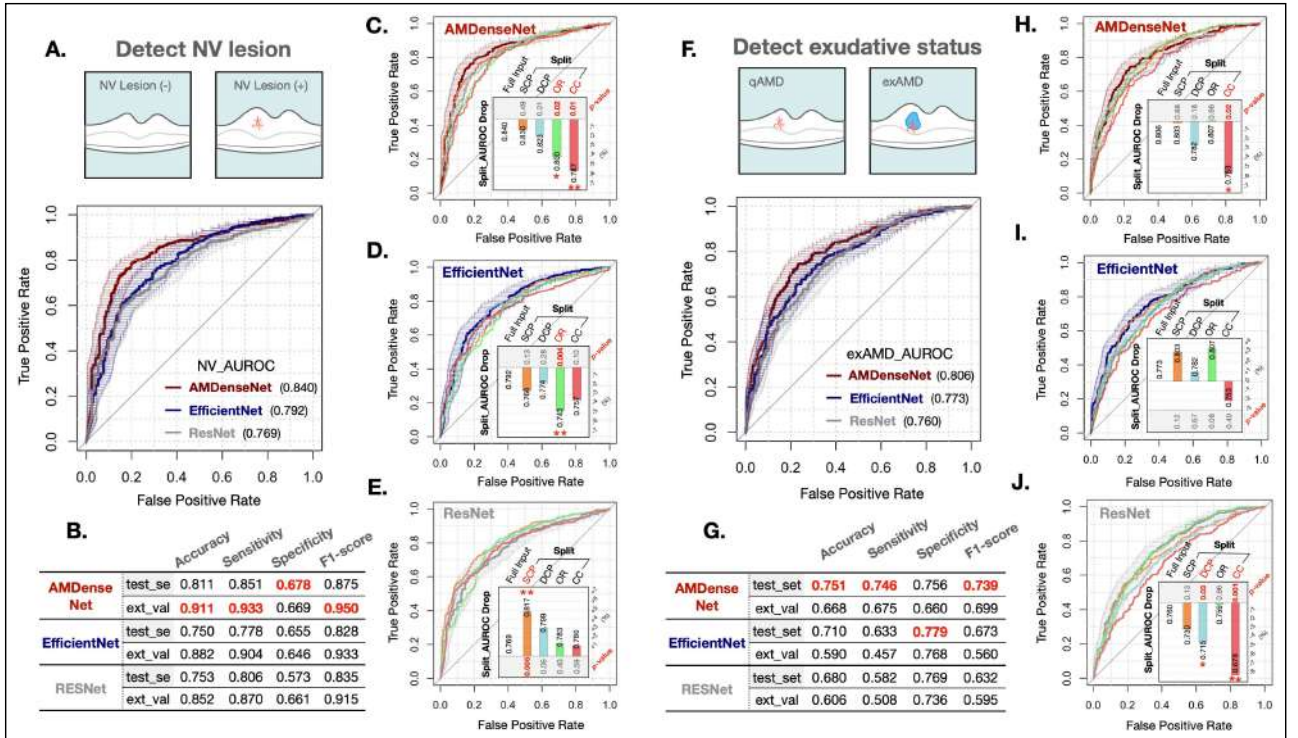


FIGURE 3 Investigation of the input split perturbation effects on model performance. (A) The merged NV detection ROC curves with 95% confidence interval (bootstrap $n = 1000$). (B) The three model NV detection performance in the test dataset and external validation dataset. (C)–(E) Measuring AUROC drop in the plexus-wise input split perturbation experiments from three NV detection models. (F) The merged exAMD detection ROC curves with 95% confidence interval (bootstrap $n = 1000$). (G) The three model exAMD detection performance in the test dataset and external validation dataset. (H)–(J) Measuring AUROC drop in the plexus-wise input split perturbation experiments from the three exAMD detection models. Footnote: The red colored digits highlight the best model performance context; the bar chart represents the degree of AUROC change; and the significant input split layers are marked in red with an asterisk (* $p < 0.05$, ** $p < 0.01$, *** $p < 0.001$).

then, plexus-wise permutation data were artificially synthesized by swapping-in a counter status plexus to the origin sequence.

$$\#(SCP_{ex}, DCP_{ex}, OR_{ex}, CC_{ex}) \bullet (SCP_q, DCP_q, OR_q, CC_q) \rightarrow (SCP_q, DCP_{ex}, OR_{ex}, CC_{ex}) + (SCP_{ex}, DCP_{ex}, OR_{ex}, CC_{ex})$$

The effect of each perturbation was evaluated by changes in area under the ROC curve (AUROC), accuracy, sensitivity (false-negative), and specificity (false-positive).

F. xAI and Its Clinical Relevance to Multimodal Images

To visualize the clinical relevance of model decisions, the xAI pixel activation map was manually registered onto the multimodal reference images to address the spatial correspondence between the model attention and the domain-specific NV features.

In the multimodal referencing process, color fundus pictures (CFPs) revealed NV hemorrhages; optic coherent tomography (OCT) revealed hypodense intraretinal and sub-retinal NV exudates; the OCT thickness map revealed the edematous landscape of the retina (color coded by population percentile rank (PR): PR < 1%: dark indigo, PR > 1%: blue,

PR > 5%: green, PR > 95%: yellow, PR > 99%: red); fluorescent angiography (FAG) revealed superficial NV exudates positioned above the pigmented epithelium, and indocyanine green angiography (ICGA) revealed deep NV exudates located beneath the pigmented epithelium.

To achieve multimodal referencing, we aligned each module to the invariant major vascular markings. Both the FAG and ICGA were resized to fit the OCTA-matched ROI. The spatial concordance between xAI pixels and NV leakage lesions was visualized by referencing the xAI results to different NV features.

III. Results

In this study, we examined the clinical applicability of AMDenseNet and InSS-P in the retinal OCTA images, then explored what pathological insights can be derived from investigating the plexus-wise vascular significance.

A. Input Split Perturbations Affect Model NV Diagnostics

Three neural networks, namely, AMDenseNet, EfficientNet, and ResNet, were trained in parallel to detect NV lesions in the OCTA test set. The merged ROC curve results (Figure 3(a)) showed that AMDenseNet (AUROC = 0.84) outperformed the standardized EfficientNet (AUROC = 0.792) and ResNet

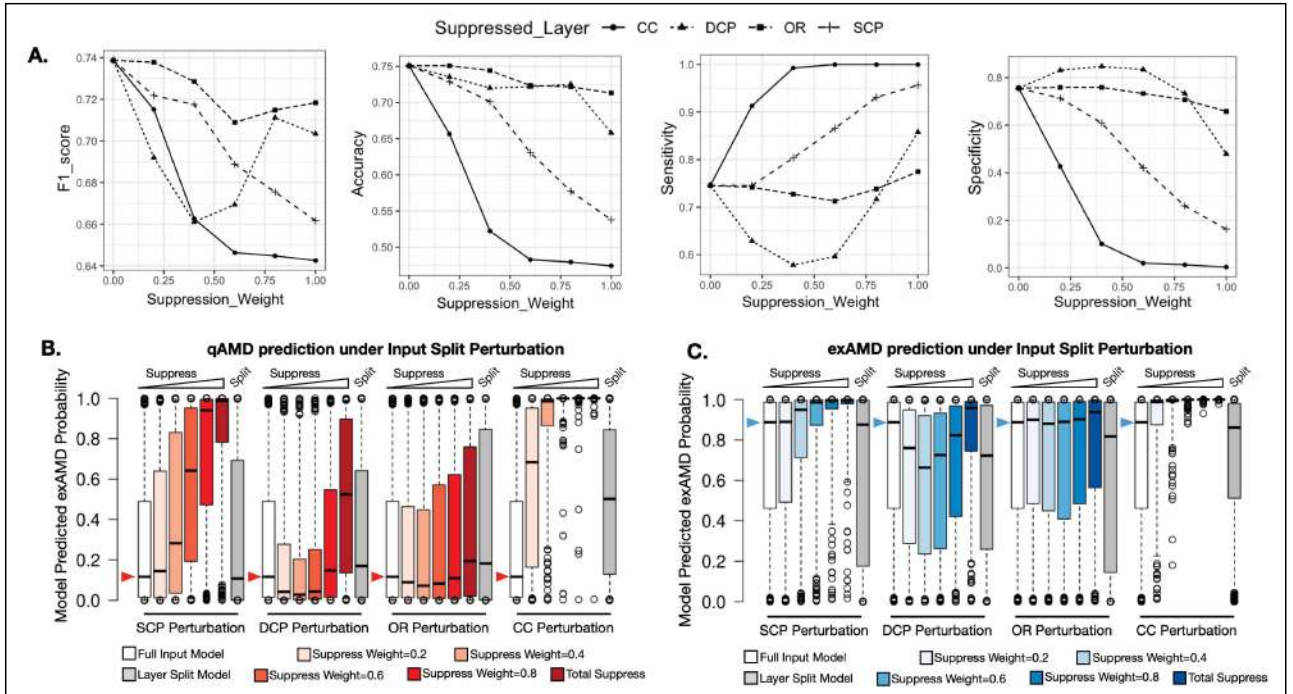


FIGURE 4 Investigation of the input suppression perturbation effects on the exAMD model detection task. (A) Line plots that recorded the AMDenseNet performance losses under plexus-wise different weighted input suppression perturbations. Box with Altman whisker plot were drawn to present the AMDenseNet predicted exAMD probability gains and losses after conducting input suppression perturbation in (B) qAMD and (C) exAMD cases.

(AUROC = 0.769) in the NV detection task. Similarly, in the external validation dataset, AMDenseNet achieved better NV detection scores (accuracy = 0.911, sensitivity = 0.933, specificity = 0.669, and F1-score = 0.95) than did the other standard models (Figure 3(b)).

To determine the marginal contribution of each anatomical input, we measured the model AUROC gap before and after plexus-wise split perturbations. Our data showed that the split-away of the OR and CC angiograms significantly compromised the AMDenseNet NV detection task ($p = 0.02$ and $p = 0.01$, respectively; Figure 3(c)). Similarly, the OR split-away impaired EfficientNet NV detection ($p = 0.04$; Figure 3(d)), whereas the SCP split-away enhanced ResNet NV detection ($p = 0.005$; Figure 3(e)). These asymmetric input influence underlined the context-dependent anatomy effects on model decisions.

The three models were compared again in the exAMD detection task (Figure 3(f)), and the AMDenseNet (AUROC = 0.806) outperformed EfficientNet (AUROC = 0.773) and ResNet (AUROC = 0.76) models in exAMD detection. Notably, AMDenseNet achieved higher exAMD detection accuracy, sensitivity and F1-scores in both the test and external validation datasets (Figure 3(g)).

The input split perturbation experiments were reiterated for exAMD detection task, and our data revealed that the CC split-away caused an unanimous performance decline in all three tested models (Figure 3(h), (i), and (j)). The CC split-away caused significant performance loss in both

AMDenseNet ($p = 0.02$) and ResNet ($p = 0.001$) models. This underlines the significance of the CC input plexus.

Based on the robustness of the AMDenseNet in NV characterization, AMDenseNet was set as the default model for subsequent perturbation experiments.

B. Input Suppression: Plexus-Wise Vascular Significance

To examine the anatomical contribution from a distinct perspective, we applied gradient suppression perturbations to generate a synthetic layer-suppressed OCTA dataset. The exAMD detection rate was plotted against the layer suppression weight (Figure 4(a)), and the results showed DCP and CC input suppression reduced the exAMD detection F1-score. By taking a closer look, the reduced exAMD F1 score was resulted from the model sensitivity loss (DCP perturbation); and model specificity loss (CC perturbation).

To further investigate the suppression-perturbation effects on model sensitivity and specificity, both qAMD and exAMD prediction results were plotted in each layer-suppression perturbation experiments. Notably, in the qAMD cases (Figure 4(b)), SCP and CC suppression led toward exAMD-like (false-positive) prediction outcome. Meanwhile, in the exAMD subgroup, DCP suppression resulted in qAMD-like (false-negative) prediction outcome (Figure 4(c)). From a clinical perspective, these findings indicated that signal suppression in the SCP and CC plexus could result in false-positive predictions (overestimation) in qAMD cases, whereas DCP

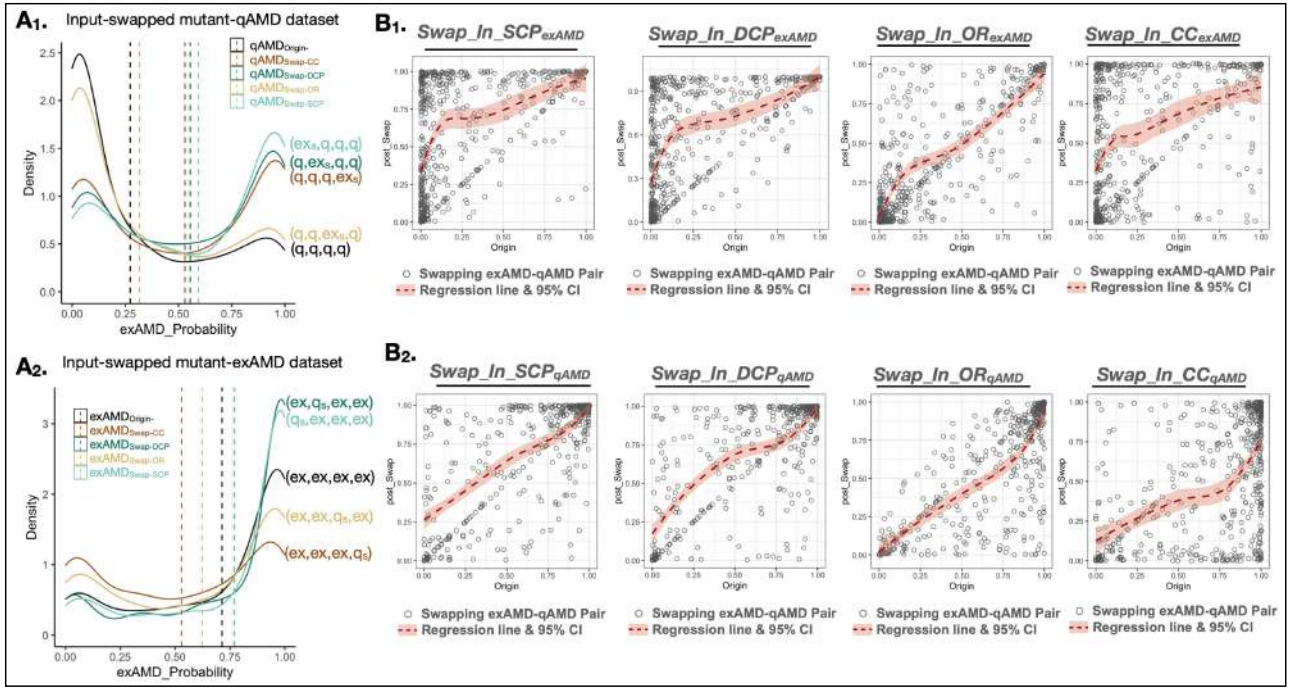


FIGURE 5 Investigation of the input swap perturbation effects on the exAMD probability gains and losses in swappable exAMD-qAMD image pairs (pairs = 583). Density plot of the model predicted exAMD scores in the wild type and single plexus mutated qAMD (A₁) and exAMD (A₂) cases. Scatter with regression line plot showed exAMD probability gains and losses after the qAMD (B₁) and exAMD (B₂) cases obtained permutation swap-in images.

suppression could lead to false-negative (underestimation) in exAMD cases.

Interestingly, our findings demonstrated a concordant trend between the anatomical split-away and suppression input perturbation. However, the suppression perturbation method generally resulted in higher exAMD estimations than the split-away perturbations.

C. Input Swap: Mutant Effects on exAMD-qAMD Detection

To further elucidate the decision-priming effects exerted by each vascular plexus, we curated a same-patient paired-up exAMD/qAMD dataset and then mated the two disease sequences in a permutation plexus swapping manner, thus deriving an array of mutant qAMD (e.g., 3x qAMD layers with 1x exAMD layer) and mutant exAMD (e.g., 3x exAMD layers with 1x qAMD layer) data.

Through analyzing the predict output discrepancy between wild-type and swap-mutated input datasets, our model decision density curve demonstrated that a single layer swap-in of the SCP_{exAMD}, DCP_{exAMD} or CC_{exAMD} plexus led towards an increased exAMD scoring of qAMD cases (Figure 5 (a₁)), whereas OR_{exAMD} plexus swap-in did not result in similar recognition dominance. On the other hand, swapping the CC_{qAMD} layer into the exAMD image sequence brought down the model predicted exAMD probability (Figure 5 (a₂)). From these two experiments, we observed that the CC anatomy possesses a strong priming effect and that the CC anatomy

anchors model attention to make CC-accordant disease impressions.

To rule out false-deducted conclusions resulting from data distribution bias, we plotted a 2D scatter plot with regression lines for the pre-swap and post-swap exAMD probabilities. In coherent to our previous findings, the CC plexus exhibited strong priming effects; CC_{exAMD} swap-in primed the qAMD sequence to form exAMD-like impressions (Figure 5 (b₁)); and CC_{qAMD} swap-in primed the exAMD sequence to form qAMD-like impressions (Figure 5 (b₂)).

Notably, the CC plexus dominance inferred from this swap-perturbation experiment was well aligned with the major conclusions of the split and suppression perturbation experiments.

D. AMDenseNet Annotates Triple-Specific (Plexus, Branch, and Activity) NV Lesions on OCTA Images

To investigate how different models behave differently under each designated input context, we applied a pixel activation map to visualize the context-dependent linkages between the anatomic features and model decisions. A sequential case-based discussion was provided to highlight the clinical relevance of each model.

In the first two AMD patients, FAG (Figures 6 (a₁) and (a₂)) revealed two distinct NV lesions with active leakage. Both patients received anti-angiogenic treatment and conferred exAMD-to-qAMD disease remission, vascular and structural changes were confirmed by multimodal image evidence

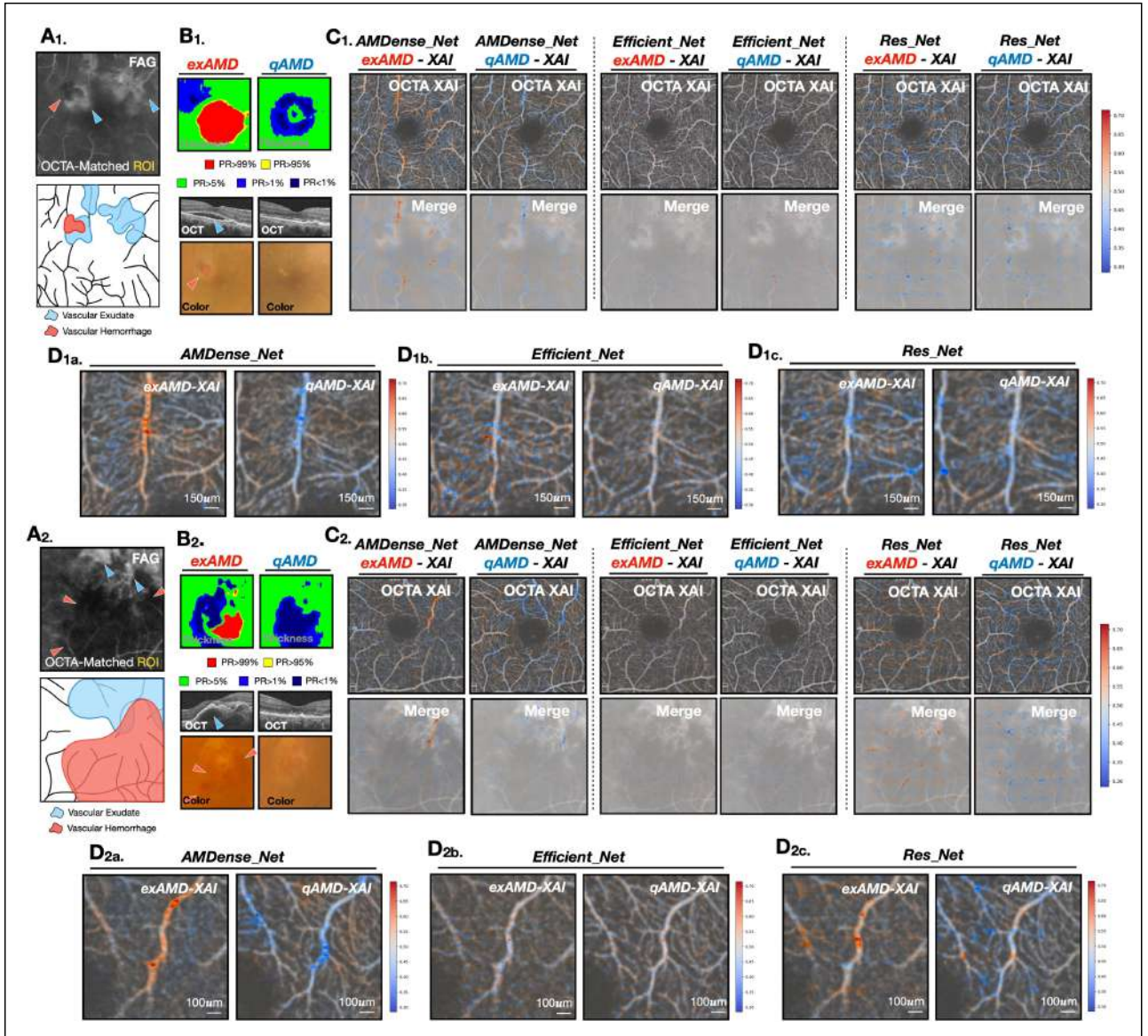


FIGURE 6 AMDenseNet xAI annotates spatio-activity resolved vascular lesions in two displayed cases. (A₁) and (A₂) FAG and illustrative figures depicted two exAMD cases with active exudation. (B₁) and (B₂) OCT thickness map, OCT cross section and color fundus pictures presented structural changes of the exAMD/qAMD disease transition. (C₁) and (C₂) OCTA model xAI pixels were overlaid on OCTA-matched FAG images, the precision and validity of model labeled NV features were evaluated by the concordance between OCTA-xAI and FAG signatures. (D₁) and (D₂) The close up view of three model xAI maps. Footnote: The blue arrow indicates retinal exudations (dye leakage), and the red arrow indicates retinal hemorrhage areas.

(thickness, retinal fluids or hemorrhage; Figures 6(b₁) and (b₂)). In these selected exAMD-qAMD disease pairs, the pixel activation xAI map was generated from OCTA inputs then overlaid with the gold standard dye-leakage FAG images (Figures 6 (c₁) and (c₂)). From the overlapped xAI-FAG signatures, the AMDenseNet xAI successfully identified NV lesions in different plexus (SCP and CC), and attributed specific vascular branches that were confirmed expressing leakage activity in the referenced FAG. Moreover, the AMDenseNet branch annotation is exAMD status-dependent, the NV lesion was marked in red for exAMD status; blue for qAMD status. Together, the AMDenseNet attributed triple-specific (plexus, branch, and activity) NV lesions on the OCTA images.

Based on a close-up view of the model activated pixels, the AMDenseNet attributed vascular lesions (Figures 6(d_{1a}) and (d_{2a})) by a much continuous and FAG-coherent manner. On the contrary, the attributed results of EfficientNet (Figure 6(d_{1b}) and (d_{2b})) and ResNet (Figure 6(d_{1c}) and (d_{2c})) were relative fragmented and presented insufficient clinical interpretability.

To further evaluate the AMDenseNet diagnostic potential in spatial OCTA cases, we studied a type 3 MNV patient with retinal exudates at two independent plexus level (Figure 7(a)). AMDenseNet xAI pixel activation highlighted an FAZ overriding NV branch that spanned across the SCP, DCP, and OR plexuses (Figure 7(b)). By double-checking the OCTA-

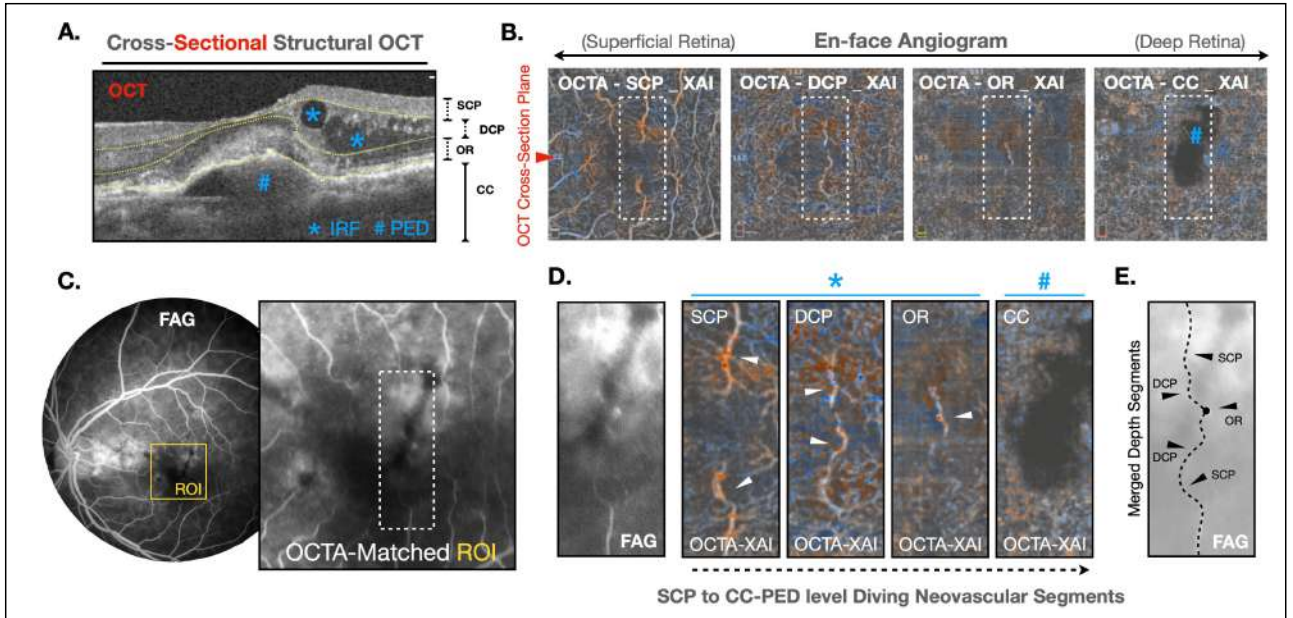


FIGURE 7 The AMDenseNet xAI attributed a reconstructable diving NV structure from the plexus-wise OCTA layers. (A) Cross-section OCT presenting a retina case with exudates in multiple depth layers. (B) The depth-resolved OCTA-xAI results highlighted a neovascular anastomosis. (C) The OCTA-matched FAG region revealed a dye-filling projection of a type 3 MNV. (D) The xAI results highlighted the independent NV segments at each layer, which reconstitutes into the diving type 3 MNV anastomosis structure. (E) A xAI-FAG merged illustration showing the plexus-wise NV segments of the type 3 MNV. Footnote: The blue asterisk (*) marks the intraretinal fluid (IRF) at the SCP and DCP levels, the blue hashtag (#) indicates the pigment epithelium detachment (PED), and the white dashed line box encircles a confined region with a diving anastomosis NV body.

matched ROI on the FAG image, an anastomosis was identified within the white-dashed line box (Figure 7(c)). Moreover, after stitching the xAI-labeled NV fragments in the SCP, DCP, and OR, the FAG-depicted NV anastomosis body was recapitulated (Figure 7(d)).

These serial cases demonstrated that the AMDenseNet xAI model has the potential to address plexus-wise microangiopathy; therefore, subsequent perturbation-xAI experiments were performed on the AMDenseNet study backbone.

E. Input Perturbations Disrupt the Clinical Relevance of Model Decisions

To probe the coupling effect between anatomical perturbations and AMDenseNet model attention, we conducted input split-away perturbations in tandem with xAI pixel activation.

The perturbation was targeted to both the superficial (SCP and DCP) and deep (CC) vasculature, and the studied cases include FAG-validated superficial NV and ICGA-validated deep NV lesions. For superficial lesions, two sets of OCTA ROI-matched color fundus and FAG images were obtained, with one representing retinal exudate conditions (Figure 8(a₁)) and the other depicting retinal hemorrhage conditions (Figure 8(a₂)). As demonstrated in the previous section, the baseline OCTA-xAI (blue arrow) attributed FAG-coherent (green arrow) NV leakage branch. We then performed subsequent perturbation-xAI experiments, and the results revealed that DCP split-away resulted in false-negative (FN) annotations at the NV lesion sites, whereas CC split-away generated strong false-positive (FP) annotations over nonspecific

vascular branches (Figures 8(b₁) and (b₂)). Taken together, the AMDenseNet xAI attributed NV characters that were comparable to gold standard dye-based leakage detection.

F. Input Perturbations Cause Context-Specific False-Negative and False-Positive Model Decisions

To examine the perturbation affected model attention in the context of exAMD-qAMD transition, the perturbation-xAI experiments were reiterated in two exAMD-qAMD disease pairs (superficial: Figure 9(a₁) and deep vascular plexus: Figure 9(a₂)).

The AMDenseNet attributed branch-specific and exAMD-specific NV lesions (blue arrow) in both the superficial and deep vascular plexuses (Figures 9(b₁) and (b₂)). Notably, in the split-DCP and split-CC perturbation experiments (Figures 9(c₁) and (c₂)), we observed that split-DCP perturbations caused false-negative (underestimation) exAMD prediction, whereas split-CC perturbations led to false-positive (overestimation) exAMD prediction. These perturbation-xAI results aligned harmonically with the discovery in the swap and suppress perturbation sections.

IV. Discussion

This study has two contributions. First, we demonstrated that a mobile-dense hybrid neural network possesses analytic advantages in medical image contents expressing high-dimensional (plexus-wise) vascular details (point-wise). Second, through the proposed input split, suppression, and swap perturbation (InSSS-P) approach, we discovered a conditioned coupling effect between anatomical inputs and model behavioral

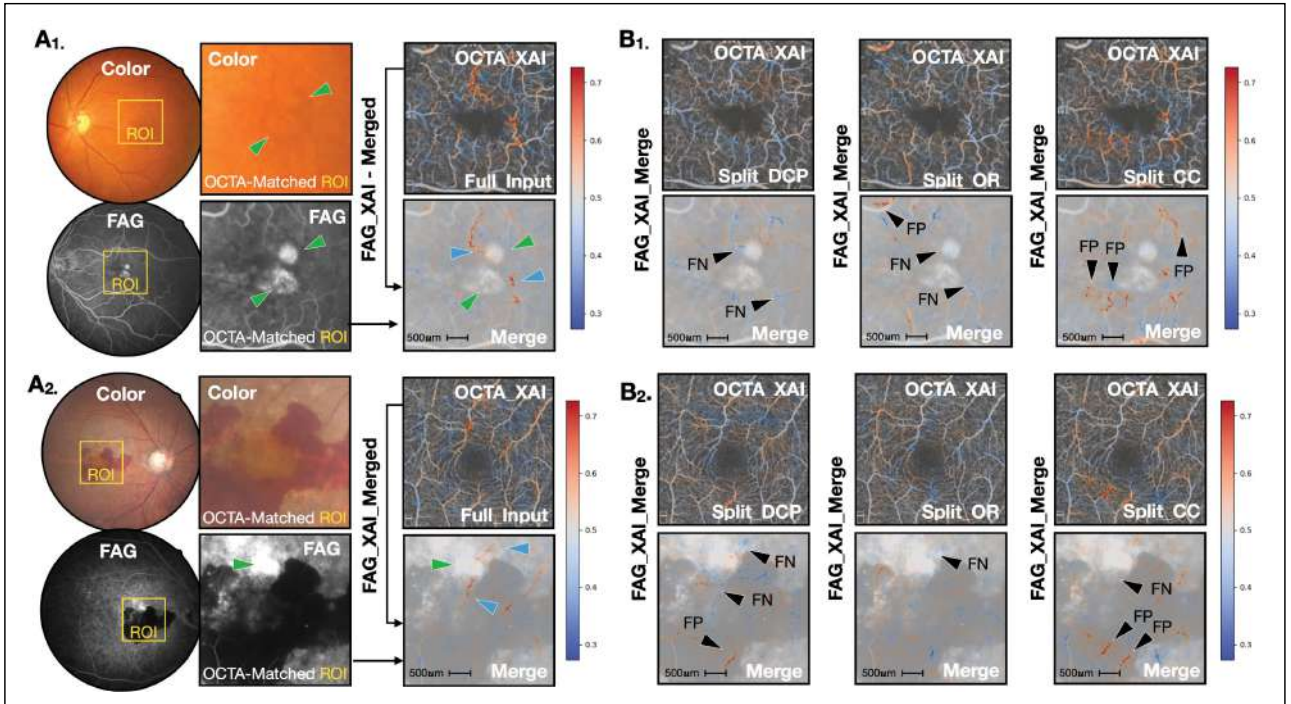


FIGURE 8 Plexus-specific input split perturbations resulted in context dependent false-negative and false-positive neovascular annotations. (A₁) and (A₂). ExAMD NV exudates, and the concordant AMDenseNet-xAI annotation were visualized and validated with multimodal referencing. (B₁) and (B₂) The plexus-wise perturbation resulted in false-positive and false-negative xAI annotations. Footnote for Figs. 8 and 9: the green arrow indicates retinal exudations (dye leakage), whereas the blue arrow indicates the XAI annotated active NV lesions. False-negative (FN) and false Positive (FP).

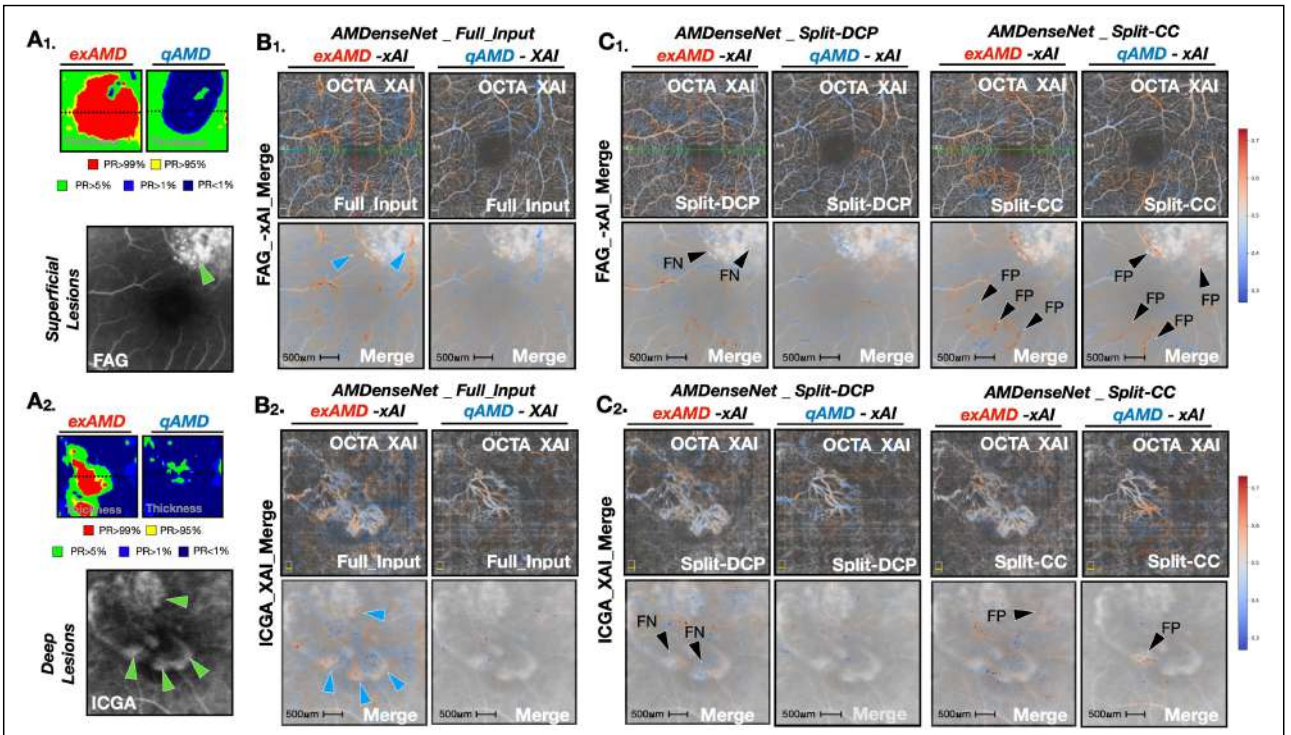


FIGURE 9 Input split perturbations abrogates model-sensibility toward disease status changes. Two exAMD-qAMD transition pairs are presented in this figure. One data pair depicted NV lesions at the superficial (SCP) level, while the other pair focused on NV lesions at deep (OR) plexus level. The thickness map with OCTA ROI-matched FAG (A₁) and ICGA (A₂) images were provided to confirm the NV location and exAMD-qAMD transition status, upon which the full input AMDenseNet-xAI annotates branch-specific and exAMD status-specific NV leakages (B₁) and (B₂). A subsequent DCP and CC input split perturbation (C₁) and (C₂) resulted in false-negative and false-positive AMDenseNet NV annotations, respectively.

outputs. In particular, DCP perturbations resulted in false-negative exAMD predictions, whereas CC perturbations contributed to false-positive exAMD predictions. This study demonstrated that InSSS-P exhibits analytic potential in adding clinical relevance to model decisions.

A. Clinical Value of the AMDenseNet

In current clinical settings, with multimodal diagnostic instruments at hand, the misdiagnosis rate of AMD remains unacceptably high, ranging from 12.5-19% [75], [76]. The misdiagnosed patients often have subclinical microangiopathy features that can only be detected by invasive dye-based angiography. Therefore, the non-invasive AMDenseNet-xAI diagnostic in OCTA uprise as an alternative framework for microangiopathy evaluation.

In the OCTA-alone diagnostic scenario, qualitative and quantitative biomarkers could detect AMD NV lesions with 67.6% sensitivity and 86.5% specificity [77]. However, our AMDenseNet NV detection results had 85.1-93.3% sensitivity and 67.8% specificity. This finding suggested that the AMDenseNet could be used to screen for microangiopathy in which NV structures are difficult to detect. In another head-to-head OCTA-FAG comparison study, OCTA detected exAMD with 50% sensitivity and 91% specificity [78]. To this end, our results demonstrated that applying AMDenseNet to OCTA images significantly improved exAMD diagnosis (sensitivity: 67.5-74.6% and specificity: 66.0-75.6%).

Ophthalmologists rely on multimodal images to characterize different aspects of NV lesions. However, as shown in Figs. 6-8, the AMDenseNet-xAI attributed triple-specific NV features (plexus, branch, and exudate activity) from a single OCTA modality. This is significant because the combination of AMDenseNet and OCTA alone recapitulates the diagnostic value of all modalities in combination. This indicated that the use of the AMDenseNet can streamline the tedious routine of longitudinal AMD follow-up.

B. Novel Insights Propelled and Confirmed by the InSSS-P

Through the InSSS-P approach, we determined that the DCP contains favorable exAMD features, while the CC plexus contains favorable qAMD characteristics. In other words, DCP perturbations result in false-negative exAMD prediction, and CC perturbations lead to false-positive exAMD prediction. On the other hand, OR perturbations did not result in significant predictive changes. Together, these findings indicated that each vascular plexus reacts asymmetrically to contextual disease cues [79], [80].

Retinal vascular homeostasis (angiogenesis and endothelial tonicity) is tightly regulated by the ocular oxygen level. While AMD is an oxidative stress disorder, NV formation is considered a compensatory physiological mechanism that provides extra oxygen to the hypoxic retina. The DCP plexus is also sensitive to oxygen dysregulation. An oxygen intervention study showed that hyperoxia (high O_2) treatment can trigger perfusion reduction and vasoconstriction in the macular DCP

[81]. ExAMD has also been shown to have reduced DCP mean perfusion density (MPD) and reduced DCP mean vascular density (MVD). Interestingly, these clinical interventional and observational studies both supported our InSSS-P-driven findings: DCP angiography contains exAMD biomarkers.

In choroid biomarker studies, peri-NV vascular signal dropout (dark halo) at the depth of the CC is a typical finding in AMD OCTA images [82], [83]. Vascular signal defects on OCTA-CC images were recently histologically confirmed as having a hypo-perfused CC status in early AMD [84]. The OCTA nonperfusion area around choroidal NV lesions was also reported to be greater in patients with exAMD than in patients with qAMD. While nonperfusion CC markers have been applied to distinguish early AMD and exAMD, our InSSS-P results revealed that the CC is a key contributor to the model's ability to detect NV lesions and predict qAMD.

The suppression of SCP and CC signals results in elevated exAMD recognition in qAMD patients (Figure 4(b)). The process of suppression perturbations blurs the vascular signals in certain plexuses, which resemble "reduced vascular density" images from the model perspective. Notably, reduced SCP vascular density has been reported in AMD patients [34] but has yet to be linked to exAMD.

C. Mobile-Dense Hybrid Application in Medical Images

MobileNet and DenseNet each have valuable traits that are suitable for medical image analysis. First, MobileNet is lightweight and cost-efficient in terms of its ability to be installed on portable medical instruments, while MobileNet excels in classification tasks [85]. Second, DenseNet employs inter-block connections to reuse convolution features and uses skip connections to enhance feature transfer without the problem of gradient vanishing [86]. Currently, a hybrid MobileNet and DenseNet structure has been applied to medical image diagnostics, including in skin cancer [87], COVID-19 chest X-rays [88], and glaucoma [89]. In these studies, the mobile-dense hybrid network outperformed its parallel models. Further medical studies on mobile-dense DNNs are warranted to fully characterize the potential of this hybrid model in medical image analysis.

D. Limitations and Perspectives

Despite the favorable results in finding novel vascular significance, our study has limitations. First, the ground truth labeling of exAMD was guided by the presence of visible fluid exudates. The eyes with fibrovascular pigment epithelium detachment without assertive ICGA confirmation were labeled non-exudative, and eyes with serous PED were excluded due to false segmentation conditions in OCTA images [90]; both conditions may underestimate the model false-negative rate. Second, we did not use NV images of patients with other disease etiologies, such as central serous chorioretinopathy [91] and diabetic retinopathy [92], [93]; therefore, whether this model could be applied to broader NV characterization tasks remains untested. Although models trained with OCTA images provide detailed vasculature profile results, it remains challenging to achieve

model accuracy levels as high as those of models developed from the mega-data of color fundus [94], [95] and OCT [20], [96] images. As OCTA is a relatively new diagnostic module with a limited amount of data, we postulate that the model performance may improve after a larger OCTA dataset becomes available.

V. Conclusion

From the technical perspective, the combination of InSSS-P and AMDenseNet reconstitutes a robust anatomy-sensible model that possesses balanced attention across global retina and local microvascular conditions. When implemented in clinical researches, this study framework could be utilized in microvascular diagnostics and angiomorphic biomarker discoveries.

Acknowledgment

Kao-Jung Chang and Shih-Hwa Chiou were affiliated with the Institute of Clinical Medicine, National Yang Ming Chiao Tung University and Department of Medical Research, Taipei Veteran General Hospital. Furthermore, the authors particularly thank Acer Medical Incorporated for providing tech support in the AI model establishment.

This work was supported in part by the National Science and Technology Council under Grant NSTC 112-2124-M-038-001, Grant NSTC 111-2314-B-075-036-MY3, and Grant NSTC 111-2314-B-075-039-MY3, and in part by Taipei Veterans General Hospital under Grant V113C-125, 113VACS-007 and Grant V113C-164, V113C-108.

References

- [1] M. Shehab et al., "Machine learning in medical applications: A review of state-of-the-art methods," *Comput. Biol. Med.*, vol. 145, 2022, Art. no. 105458.
- [2] G. Varoquaux and V. Cheplygina, "Machine learning for medical imaging: Methodological failures and recommendations for the future," *npj Digit. Med.*, vol. 5, no. 1, 2022, Art. no. 48.
- [3] A. Lavecchia, "Deep learning in drug discovery: Opportunities, challenges and future prospects," *Drug Discov. Today*, vol. 24, no. 10, pp. 2017–2032, 2019.
- [4] J. Y. Ryu, H. U. Kim, and S. Y. Lee, "Deep learning improves prediction of drug–drug and drug–food interactions," *Proc. Nat. Acad. Sci. USA*, vol. 115, no. 18, pp. E4304–E4311, May 2018.
- [5] M. K. K. Niazi, A. V. Parwani, and M. N. Gurcan, "Digital pathology and artificial intelligence," *Lancet Oncol.*, vol. 20, no. 5, pp. e253–e261, May 2019.
- [6] A. Janowczyk and A. Madabhushi, "Deep learning for digital pathology image analysis: A comprehensive tutorial with selected use cases," *J. Pathol. Inform.*, vol. 7, 2016, Art. no. 29.
- [7] S. Benjamins, P. Dhunoo, and B. Meskó, "The state of artificial intelligence-based FDA-approved medical devices and algorithms: An online database," *NPJ Digit. Med.*, vol. 3, 2020, Art. no. 118.
- [8] M. Nagendran et al., "Artificial intelligence versus clinicians: Systematic review of design, reporting standards, and claims of deep learning studies," *Bmj*, vol. 368, Mar. 2020, Art. no. m689.
- [9] A. Mishra, "Transparent AI: Reliabilist and proud," *J. Med. Ethics*, vol. 47, pp. 341–342, Apr. 2021.
- [10] A. Barredo Arrieta, "Explainable artificial intelligence (XAI): Concepts, taxonomies, opportunities and challenges toward responsible AI," *Inf. Fusion*, vol. 58, pp. 82–115, 2020.
- [11] D. Sacks, "Multisociety consensus quality improvement revised consensus statement for endovascular therapy of acute ischemic stroke," *Int. J. Stroke*, vol. 13, no. 6, pp. 612–632, Aug. 2018.
- [12] M. Ivanovs, R. Kadikis, and K. Ozols, "Perturbation-based methods for explaining deep neural networks: A survey," *Pattern Recognit. Lett.*, vol. 150, pp. 228–234, 2021.
- [13] I. Hameed et al., "BASED-XAI: Breaking ablation studies down for explainable artificial intelligence," Sep. 2022, *arXiv:2207.05566*.
- [14] M. D. Zeiler and R. Fergus, "Visualizing and understanding convolutional networks," in *Proc. 13th Eur. Conf. Comput. Vis.*, 2014, pp. 818–833.
- [15] V. Petsiuk, A. Das, and K. Saenko, "RISE: Randomized input sampling for explanation of black-box models," Sep. 2018, *arXiv:1806.07421*.

- [16] M. T. Ribeiro, S. Singh, and C. Guestrin, "'Why should I trust you?': Explaining the predictions of any classifier," in *Proc. 22nd ACM SIGKDD Int. Conf. Knowl. Discov. Data Mining*, 2016, pp. 1135–1144.
- [17] S. Lundberg and S.-I. Lee, "A unified approach to interpreting model predictions," in *Proc. 31st Int. Conf. Neural Inf. Process. Syst.*, May 2017, pp. 4768–4777.
- [18] S. Hooker, D. Erhan, P.-J. Kindermans, and B. Kim, "A benchmark for interpretability methods in deep neural networks," in *Proc. 33rd Int. Conf. Neural Inf. Process. Syst.*, Jun. 2019, pp. 9737–9748.
- [19] Z. Salahuddin, H. C. Woodruff, A. Chatterjee, and P. Lambin, "Transparency of deep neural networks for medical image analysis: A review of interpretability methods," *Comput. Biol. Med.*, vol. 140, 2022, Art. no. 105111.
- [20] D. S. Kermany et al., "Identifying medical diagnoses and treatable diseases by image-based deep learning," *Cell*, vol. 172, no. 5, pp. 1122–1131.e9, 2018.
- [21] Z. Tang et al., "Interpretable classification of Alzheimer's disease pathologies with a convolutional neural network pipeline," *Nature Commun.*, vol. 10, no. 1, 2019, Art. no. 2173.
- [22] G. Quellec, H. Al Hajj, M. Lamard, P.-H. Conze, P. Massin, and B. Cochener, "ExplAIIn: Explanatory artificial intelligence for diabetic retinopathy diagnosis," *Med. Image Anal.*, vol. 72, 2021, Art. no. 102118.
- [23] R. Fong, M. Patrick, and A. Vedaldi, "Understanding deep networks via extremal perturbations and smooth masks," in *Proc. IEEE/CVF Int. Conf. Comput. Vis.*, 2019, pp. 2950–2958.
- [24] Q. Yang, X. Zhu, J. Fwu, Y. Ye, G. You, and Y. Zhu, "MFPP: Morphological fragmental perturbation pyramid for black-box model explanations," in *Proc. 25th Int. Conf. Pattern Recognit.*, 2021, pp. 1376–1383.
- [25] A. Ghorbani, A. Abid, and J. Zou, "Interpretation of neural networks is fragile," in *Proc. AAAI Conf. Artif. Intell.*, 2019, vol. 33, no. 01, pp. 3681–3688.
- [26] D. Slack, S. Hilgard, S. Singh, and H. Lakkaraju, "Reliable post hoc explanations: Modeling uncertainty in explainability," in *Proc. Adv. Neural Inf. Process. Syst.*, Aug. 2020, pp. 9391–9404.
- [27] A.-K. Dombrowski, M. Alber, C. J. Anders, M. Ackermann, K.-R. Müller, and P. Kessel, "Explanations can be manipulated and geometry is to blame," in *Proc. 33rd Int. Conf. Neural Inf. Process. Syst.*, 2019, Art. no. 1217.
- [28] J. Adebayo, J. Gilmer, M. Muelly, I. Goodfellow, M. Hardt, and B. Kim, "Sanity checks for saliency maps," in *Proc. 32nd Int. Conf. Neural Inf. Process. Syst.*, 2018, pp. 9525–9536.
- [29] T. E. de Carlo, A. Romano, N. K. Waheed, and J. S. Duker, "A review of optical coherence tomography angiography (OCTA)," *Int. J. Retina Vitreous*, vol. 1, no. 1, 2015, Art. no. 5.
- [30] B. Zhang, Y. Chou, X. Zhao, J. Yang, and Y. Chen, "Early detection of microvascular impairments with optical coherence tomography angiography in diabetic patients without clinical retinopathy: A meta-analysis," *Amer. J. Ophthalmol.*, vol. 222, pp. 226–237, 2021.
- [31] D. M. Sampson, A. M. Dubis, F. K. Chen, R. J. Zawadzki, and D. D. Sampson, "Toward standardizing retinal optical coherence tomography angiography: A review," *Light: Sci. Appl.*, vol. 11, no. 1, 2022, Art. no. 63.
- [32] Y. Jia et al., "Split-spectrum amplitude-decorrelation angiography with optical coherence tomography," *Opt. Exp.*, vol. 20, no. 4, pp. 4710–4725, 2012.
- [33] Q. S. You et al., "Detection of reduced retinal vessel density in eyes with geographic atrophy secondary to age-related macular degeneration using projection-resolved optical coherence tomography angiography," *Amer. J. Ophthalmol.*, vol. 209, pp. 206–212, 2020.
- [34] M. Trinh, M. Kalloniatis, and L. Nivison-Smith, "Vascular changes in intermediate age-related macular degeneration quantified using optical coherence tomography angiography," *Transl. Vis. Sci. Technol.*, vol. 8, no. 4, pp. 20–20, 2019.
- [35] C. Florence et al., "Optical coherence tomography angiography in exudative age-related macular degeneration: A predictive model for treatment decisions," *Brit. J. Ophthalmol.*, vol. 103, no. 9, 2019, Art. no. 1342.
- [36] C.-R. Hsu, T.-T. Lai, Y.-T. Hsieh, T.-C. Ho, C.-M. Yang, and C.-H. Yang, "Combined quantitative and qualitative optical coherence tomography angiography biomarkers for predicting active neovascular age-related macular degeneration," *Sci. Rep.*, vol. 11, no. 1, 2021, Art. no. 18068.
- [37] D. Hanumunthadu et al., "Biomarkers of macular neovascularisation activity using optical coherence tomography angiography in treated stable neovascular age related macular degeneration," *BMC Ophthalmol.*, vol. 23, no. 1, 2023, Art. no. 68.
- [38] G. Cennamo, D. Montorio, A. D'Alessandro, P. Napolitano, L. D'Andrea, and F. Tranfa, "Prospective study of vessel density by optical coherence tomography angiography after intravitreal bevacizumab in exudative age-related macular degeneration," *Ophthalmol. Ther.*, vol. 9, no. 1, pp. 77–85, 2020.
- [39] S. C. Lee et al., "Retinal vessel density in exudative and nonexudative age-related macular degeneration on optical coherence tomography angiography," *Amer. J. Ophthalmol.*, vol. 212, pp. 7–16, Apr. 2020.
- [40] C.-H. Huang, P.-T. Yeh, Y.-T. Hsieh, T.-C. Ho, C.-M. Yang, and C.-H. Yang, "Characterizing branching vascular network morphology in polypoidal choroidal vasculopathy by optical coherence tomography angiography," *Sci. Rep.*, vol. 9, no. 1, 2019, Art. no. 595.
- [41] S. Torcato et al., "Swept-source OCTA quantification of capillary closure predicts ETDRS severity staging of NPDR," *Brit. J. Ophthalmol.*, vol. 106, no. 5, 2022, Art. no. 712.
- [42] T. T. Hormel, T. S. Hwang, S. T. Bailey, D. J. Wilson, D. Huang, and Y. Jia, "Artificial intelligence in OCT angiography," *Prog. Retinal Eye Res.*, vol. 85, 2021, Art. no. 100965.

- [43] Q. Yan et al., "Deep-learning-based prediction of late age-related macular degeneration progression," *Nature Mach. Intell.*, vol. 2, no. 2, pp. 141–150, 2020.
- [44] D. K. Hwang et al., "Artificial intelligence-based decision-making for age-related macular degeneration," *Theranostics*, vol. 9, no. 1, pp. 232–245, 2019.
- [45] L. Dai et al., "A deep learning system for detecting diabetic retinopathy across the disease spectrum," *Nature Commun.*, vol. 12, no. 1, 2021, Art. no. 3242.
- [46] V. Gulshan et al., "Development and validation of a deep learning algorithm for detection of diabetic retinopathy in retinal fundus photographs," *Jama*, vol. 316, no. 22, pp. 2402–2410, Dec. 2016.
- [47] D. Gao, N. Celik, X. Wu, B. M. Williams, A. Stylianides, and Y. Zheng, "A novel deep learning based OCTA destriping method," in *Proc. 23rd Conf. Med. Image Understanding Anal.*, 2020, pp. 189–197.
- [48] A. Li, C. Du, and Y. Pan, "Deep-learning-based motion correction in optical coherence tomography angiography," *J. Biophotonics*, vol. 14, no. 12, Dec. 2021, Art. no. e202100097.
- [49] Y. Liu et al., "Disentangled representation learning for OCTA vessel segmentation with limited training data," *IEEE Trans. Med. Imag.*, vol. 41, no. 12, pp. 3686–3698, Dec. 2022.
- [50] X. Wang, H. Chen, S. Tang, Z. Wu, and W. Zhu, "Disentangled representation learning," Nov. 2022, *arXiv:2211.11695*.
- [51] L. David, S. Taeyoon, K. Tae-Hoon, A. Mansour, A. Tobiloba, and Y. Xincheng, "Retinal vascular connectivity network for deep learning OCTA construction from single OCT volume scan," *Proc. SPIE*, vol. 12360, Mar. 2023, Art. no. 1236003.
- [52] R. A. Alshareef et al., "Segmentation errors in macular ganglion cell analysis as determined by optical coherence tomography in eyes with macular pathology," *Int. J. Retina Vitreous*, vol. 3, no. 1, 2017, Art. no. 25.
- [53] Q. Li et al., "DeepRetina: Layer segmentation of retina in OCT images using deep learning," *Transl. Vis. Sci. Technol.*, vol. 9, no. 2, 2020, Art. no. 61.
- [54] L. Lin et al., "BSDA-Net: A boundary shape and distance aware joint learning framework for segmenting and classifying OCTA images," in *Proc. Med. Image Comput. Assist. Intervention*, 2021, pp. 65–75.
- [55] S. Liu et al., "Polar-Net: A clinical-friendly model for alzheimer's disease detection in OCTA Images," *Lecture Notes Comput. Sci.*, pp. 607–617, Jan. 2023.
- [56] J. L. Lauer, M. Treder, M. Alnawaiseh, C. R. Clemens, N. Eter, and F. Alten, "Automated OCT angiography image quality assessment using a deep learning algorithm," *Graefes Arch. Clin. Exp. Ophthalmol.*, vol. 257, no. 8, pp. 1641–1648, 2019.
- [57] R. M. Dhodapkar, E. Li, K. Nwanyanwu, R. Adelman, S. Krishnaswamy, and J. C. Wang, "Deep learning for quality assessment of optical coherence tomography angiography images," *Sci. Rep.*, vol. 12, no. 1, 2022, Art. no. 13775.
- [58] M. Gao, Y. Guo, T. T. Hormel, J. Sun, T. S. Hwang, and Y. Jia, "Reconstruction of high-resolution 6×6-mm OCT angiograms using deep learning," *Biomed. Opt. Exp.*, vol. 11, no. 7, pp. 3585–3600, 2020.
- [59] D. Yang et al., "Deep learning in optical coherence tomography angiography: Current progress, challenges, and future directions," *Diagnostics*, vol. 13, 2023, Art. no. 326.
- [60] M. Alam, D. Le, T. Son, J. I. Lim, and X. Yao, "AV-Net: Deep learning for fully automated artery-vein classification in optical coherence tomography angiography," *Biomed. Opt. Exp.*, vol. 11, no. 9, pp. 5249–5257, 2020.
- [61] M. Abtahi, D. Le, J. I. Lim, and X. Yao, "MF-AV-Net: An open-source deep learning network with multimodal fusion options for artery-vein segmentation in OCT angiography," *Biomed. Opt. Exp.*, vol. 13, no. 9, pp. 4870–4888, Sep. 2022.
- [62] T. Adejumo, T.-H. Kim, D. Le, T. Son, G. Ma, and X. Yao, "Depth-resolved vascular profile features for artery-vein classification in OCT and OCT angiography of human retina," *Biomed. Opt. Exp.*, vol. 13, no. 2, pp. 1121–1130, 2022.
- [63] Z. Liang, J. Zhang, and C. An, "Foveal avascular zone segmentation of OCTA images using deep learning approach with unsupervised vessel segmentation," in *Proc. IEEE Int. Conf. Acoust., Speech Signal Process.*, 2021, pp. 1200–1204.
- [64] Y. Guo et al., "Quantification of nonperfusion area in montaged widefield OCT angiography using deep learning in diabetic retinopathy," *Ophthalmol. Sci.*, vol. 1, no. 2, Jun. 2021, Art. no. 100027.
- [65] J. Hao et al., "Retinal structure detection in OCTA image via voting-based multitask learning," *IEEE Trans. Med. Imag.*, vol. 41, no. 12, pp. 3969–3980, Dec. 2022.
- [66] D. Nagasato et al., "Automated detection of a nonperfusion area caused by retinal vein occlusion in optical coherence tomography angiography images using deep learning," *PLoS One*, vol. 14, no. 11, 2019, Art. no. e0223965.
- [67] G. Ryu, K. Lee, D. Park, S. H. Park, and M. Sagong, "A deep learning model for identifying diabetic retinopathy using optical coherence tomography angiography," *Sci. Rep.*, vol. 11, no. 1, 2021, Art. no. 23024.
- [68] P. Zang, T. T. Hormel, T. S. Hwang, S. T. Bailey, D. Huang, and Y. Jia, "Deep-learning-aided diagnosis of diabetic retinopathy, age-related macular degeneration, and glaucoma based on structural and angiographic OCT," *Ophthalmol. Sci.*, vol. 3, no. 1, 2023, Art. no. 100245.
- [69] A. G. Howard et al., "MobileNets: Efficient convolutional neural networks for mobile vision applications," 2017, *arXiv:1704.04861*.
- [70] G. Huang, Z. Liu, L. V. D. Maaten, and K. Q. Weinberger, "Densely connected convolutional networks," in *Proc. IEEE Conf. Comput. Vis. Pattern Recognit.*, 2017, pp. 2261–2269.
- [71] M. Tan and Q. V. Le, "EfficientNet: Rethinking model scaling for convolutional neural networks," in *Proc. Int. Conf. Mach. Learn.*, May 2019, pp. 6105–6114.
- [72] K. He, X. Zhang, S. Ren, and J. Sun, "Deep residual learning for image recognition," in *Proc. IEEE Conf. Comput. Vis. Pattern Recognit.*, 2016, pp. 770–778.
- [73] D. P. Kingma and J. Ba, "Adam: A method for stochastic optimization," Dec. 2014, *arXiv:1412.6980*.
- [74] M. Sundararajan, A. Taly, and Q. Yan, "Axiomatic attribution for deep networks," in *Proc. 34th Int. Conf. Mach. Learn.*, 2017, vol. 70, pp. 3319–3328.
- [75] A. Ozkaya, R. Garip, H. Nur Tarakcioglu, Z. Alkin, and M. Taskapili, "Clinical and imaging findings of pattern dystrophy subtypes; diagnostic errors and unnecessary treatment in clinical practice," *J. Français d'Ophthalmologie*, vol. 41, no. 1, pp. 21–29, 2018.
- [76] E. Borrelli et al., "Rate of misdiagnosis and clinical usefulness of the correct diagnosis in exudative neovascular maculopathy secondary to AMD versus pachychoroid disease," *Sci. Rep.*, vol. 10, no. 1, 2020, Art. no. 20344.
- [77] J. Gong, S. Yu, Y. Gong, F. Wang, and X. Sun, "The diagnostic accuracy of optical coherence tomography angiography for neovascular age-related macular degeneration: A comparison with fundus fluorescein angiography," *J. Ophthalmol.*, vol. 2016, 2016, Art. no. 7521478.
- [78] T. E. De Carlo et al., "Spectral-domain optical coherence tomography angiography of choroidal neovascularization," *Ophthalmology*, vol. 122, no. 6, pp. 1228–1238, Jun. 2015.
- [79] J. J. Park, B. T. Soetikno, and A. A. Fawzi, "Characterization of the middle capillary plexus using optical coherence tomography angiography in healthy and diabetic eyes," *Retina*, vol. 36, no. 11, pp. 2039–2050, 2016.
- [80] Q. Zhu et al., "Characterization of the three distinct retinal capillary plexuses using optical coherence tomography angiography in myopic eyes," *Transl. Vis. Sci. Technol.*, vol. 9, no. 4, pp. 8–20, Mar. 2020.
- [81] N. Hommer et al., "Effect of hyperoxia and hypoxia on retinal vascular parameters assessed with optical coherence tomography angiography," *Acta Ophthalmologica*, vol. 100, no. 6, pp. e1272–e1279, 2022.
- [82] Y. Jia et al., "Quantitative optical coherence tomography angiography of choroidal neovascularization in age-related macular degeneration," *Ophthalmology*, vol. 121, no. 7, pp. 1435–1444, 2014.
- [83] C. M. Keiner et al., "Quantifying choriocapillaris hypoperfusion in patients with choroidal neovascularization using swept-source OCT angiography," *Clin. Ophthalmol.*, vol. 13, pp. 1613–1620, 2019.
- [84] G. A. Luty, D. S. McLeod, I. A. Bhattu, M. M. Edwards, and J. M. Seddon, "Choriocapillaris dropout in early age-related macular degeneration," *Exp. Eye Res.*, vol. 192, Mar. 2020, Art. no. 107939.
- [85] W. Wang, Y. Li, T. Zou, X. Wang, J. You, and Y. Luo, "A novel image classification approach via dense-MobileNet models," *Mobile Inf. Syst.*, vol. 2020, 2020, Art. no. 7602384.
- [86] T. Zhou, X. Ye, H. Lu, X. Zheng, S. Qiu, and Y. Liu, "Dense convolutional network and its application in medical image analysis," *BioMed Res. Int.*, vol. 2022, 2022, Art. no. 2384830.
- [87] D. Keerthana, V. Venugopal, M. K. Nath, and M. Mishra, "Hybrid convolutional neural networks with SVM classifier for classification of skin cancer," *Biomed. Eng. Adv.*, vol. 5, 2023, Art. no. 100069.
- [88] H. Gupta, N. Bansal, S. Garg, H. Mallik, A. Prabha, and J. Yadav, "A hybrid convolutional neural network model to detect COVID-19 and pneumonia using chest X-ray images," *Int. J. Imag. Syst. Technol.*, vol. 33, no. 1, pp. 39–52, 2023.
- [89] F. J. Xavier and F. F. F. "ODMNet: Automated glaucoma detection and classification model using heuristically aided optimized DenseNet and MobileNet transfer learning," *Cybernet. Syst.*, vol. 55, pp. 245–277, 2023.
- [90] A. Au et al., "Volumetric analysis of vascularized serous pigment epithelial detachment progression in neovascular age-related macular degeneration using optical coherence tomography angiography," *Invest. Ophthalmol. Vis. Sci.*, vol. 60, no. 10, pp. 3310–3319, 2019.
- [91] M. A. Bonini Filho et al., "Association of choroidal neovascularization and central serous chorioretinopathy with optical coherence tomography angiography," *JAMA Ophthalmol.*, vol. 133, no. 8, pp. 899–906, Aug. 2015.
- [92] B. Tan et al., "Quantitative microvascular analysis with wide-field optical coherence tomography angiography in eyes with diabetic retinopathy," *JAMA Netw. Open*, vol. 3, no. 1, 2020, Art. no. e1919469.
- [93] A. Arrigo et al., "Macular neovascularization in AMD, CSC and best vitelliform macular dystrophy: Quantitative OCTA detects distinct clinical entities," *Eye*, vol. 35, no. 12, pp. 3266–3276, 2021.
- [94] F. Grassmann et al., "A deep learning algorithm for prediction of age-related eye disease study severity scale for age-related macular degeneration from color fundus photography," *Ophthalmology*, vol. 125, no. 9, pp. 1410–1420, 2018.
- [95] P. M. Burlina, N. Joshi, M. Pekala, K. D. Pacheco, D. E. Freund, and N. M. Bressler, "Automated grading of age-related macular degeneration from color fundus images using deep convolutional neural networks," *JAMA Ophthalmol.*, vol. 135, no. 11, pp. 1170–1176, Nov. 2017.
- [96] J. Yim et al., "Predicting conversion to wet age-related macular degeneration using deep learning," *Nature Med.*, vol. 26, no. 6, pp. 892–899, 2020.